Rare Metal Materials and Engineering
Volume 55, Issue 9, September 2026
Available online at www.rmme.ac.cn

Science Press

Cite this article as: Berezner Arseniy Dmitrievich, Fedorov Victor Alexandrovich, Perov Nikolai Sergeevich, et al. Non-isothermal Flow of Al-, Co-, and Cu-based Alloys of Different Spatial Configurations or Structural States: Model Establishment and Experiment[J]. Rare Metal Materials and Engineering, 2026, 55(09): 2179-2187. DOI: https://doi.org/10.12442/j.issn.1002-185X.20250585.

ARTICLE

Non-isothermal Flow of Al-, Co-, and Cu-based Alloys of Different Spatial Configurations or Structural States: Model Establishment and Experiment

Berezner Arseniy Dmitrievich[1], Fedorov Victor Alexandrovich[1], Perov Nikolai Sergeevich[2], Qiao Jichao[3], Gromov Victor Evgenievich[4], Zadorozhnyy Mikhail Yurievich[5], Gregory Victorovich Grigoriev[1]

[1] Theoretical and Experimental Physics Department, Derzhavin Tambov State University, Tambov 392000, Russia; [2] Magnetism Department, Lomonosov Moscow State University, Moscow 119991, Russia; [3] School of Mechanics and Transportation Engineering, Northwestern Polytechnical University, Xi'an 710072, China; [4] Department of Natural Sciences, Siberian State Industrial University, Novokuznetsk 654007, Russia; [5] Laboratory of Functional Polymeric Materials, National University of Science and Technology "MISIS", Moscow 119049, Russia

Abstract: The universal generalizing approach for non-isothermal behaviour of different alloys was provided with the novel deformation modelling. Results show that strong correlation can be found between the predicted model and experiment results, which shows accurate estimation of main applied parameters, such as the linear thermal expansion coefficient. Necking contours and critical thickness at corrugation for ribbon and rod specimens can also be calculated. Fractal analysis of corrugation folds (their main size) was conducted for polycrystalline and amorphous ribbon specimens. Structural peculiarities at the plastic deformation stage were investigated.

Key words: metallic glasses; thermal analysis; thermal expansion; scanning electron microscope

1 Introduction

Study of elastic and plastic deformation is an essential, useful, and well-known approach in different fields of fundamental and applied science[1–6]. Each specimen exhibits a unique response depending on its initial and boundary deformation conditions[7]. Particularly, temporally increasing axial load leads to linear deformation of amorphous alloys until fracture[8], but the same conditions contribute to a noticeable strain hardening for polycrystalline specimens[9] accompanied by the further accelerating necking and final fracture. In addition, more complex (non-linear) stretching behaviour can occur in the alloys, such as auxetics[10], due to chemical composition or interatomic arrangements. Another example of the system sensitivity to external conditions is the response to thermal impact. Isothermal loading mode for metallic alloys (i. e., heat transfer at non-room temperature) can lead to additional local structure reorganizations[11], and uniformly increasing the thermal impact contributes to the change in the experimental curve[12]. Cyclic force loading at constant or variable temperatures[13–14] as well as loading under different conditions (stretching or bending) [15] can distinctly affect deformation dynamics.

Isochronal dilatation regime[16] is qualitatively identical to the thermal mechanical analysis (TMA) [17] due to similar deformation dynamics at static external loading[13]. Normally, the primary driver of deformation is gravity; but in TMA, a preset automatic force, which is controlled by the bottom grip of the testing machine, is used. In both experiment modes, except for mechanical loading, additional acceleration of the

Received date: November 14, 2025
Corresponding author: Berezner Arseniy Dmitrievich, Ph. D., Theoretical and Experimental Physics Department, Derzhavin Tambov State University, Tambov 392000, Russia, E-mail: a. berezner1009@gmail. com; Qiao Jichao, Ph. D., Professor, School of Mechanics and Transportation Engineering, Northwestern Polytechnical University, Xi'an 710072, P. R. China, E-mail: qjczy@nwpu.edu.cn

process is provided by temporally uniform heating. This similarity in deformation regime requires further analysis from the quantitative model standpoint, because a complex study may simplify predictions of the sample response at different conditions, such as chemical composition and interatomic bonding. It is worth noting that non-isothermal behaviour remains theoretically understudied, despite its intensive experimental investigation[18]. Thus, isothermal deformation has been properly investigated mostly at the elasto-plastic stage[19], where the exponential viscoelastic material model is used[7]. Moreover, in traditional (isothermal) creep theory[20–22], deformation is mainly considered for polycrystalline alloys with respect to grain boundaries and dislocation mechanisms[23], which can be conceptually non-effective (or even erroneous) for the description of deformation in amorphous alloys due to their disordered structure[24]. In addition to dislocation models, various alternative approaches can be used to describe the metallic glasses (MGs), including free volume[25], shear bands[26], flow units[27], quasi-point defect theory[28], and thermodynamic theory[29].

During plastic deformation and fracture, fatigue is an important factor to describe necking phenomena[30] or corrugation phenomena for thin specimens[31]. At variable temperatures[32], the model analysis is complicated by non-linear boundary conditions, which requires new approaches.

Combined with the noted non-isothermal deformation features, a novel universal description of TMA, namely dynamic-mechanical analysis (DMA) and isochronal testing, for Al- , Co- , and Cu-based amorphous or polycrystalline alloys was discussed. The thermodynamic[29] and deformation[33–35] models were jointly used. In this research, the deformation fracture features of plane and cylinder alloys were investigated. A critical thickness of the specimens at initial and necking release stages was estimated.

2 Experiment

Amorphous Al-Y-Ni-Co ($Al_{85}Y_8Ni_5Co_2$), Cu-Pd-P ($Cu_{54}Pd_{28}P_{18}$), and Co-Fe-Si-Mn-B-Cr (like widespread VAC6150, VAC6030, VAC6070, and MG2714 Vacuumschmelze/Metglass alloys) ribbon MGs were chosen as testing specimens. Additionally, industrial polycrystalline Al-Fe (98wt% Al and 2wt% Fe) ribbons and copper rods were also used for comparison. Phase composition[36–37] of materials was estimated by X-ray diffractometer (XRD, Bruker D2 Phaser with Cu Kα radiation), and the results are shown in Fig.1.

Thermomechanical analysis of Al-Y-Ni-Co and Cu-Pd-P ribbon MGs was performed by Q800 testing machine under external load of 3 MPa, heating rate of 5 K/min, and designed heating temperature of 673 K. Working sizes of Al-Y-Ni-Co amorphous specimens were about 16.5, 1.4, and 0.02 mm in length, width, and thickness, respectively; working sizes of Cu-based MGs were 16.5, 2.5, and 0.025 mm in length, width, and thickness, respectively. DMA was also conducted on Q800 device at similar experimental conditions but in elastic harmonic oscillation mode (loading frequency of 3 Hz, loading stress of 3 MPa, and static preloading stress of 12 MPa) at 540 K. Non-isothermal creep behaviour of Co-Fe-Si-Mn-B-Cr MGs and polycrystalline Al-Fe or Cu-based alloys was studied using a Riftek triangle laser sensor at natural static gravity load of 1 N (i.e., stress of 14 MPa) and heating rate of 1 K/s. A typical loading scheme is shown in Fig. 2. However, the sizes of Al-Fe crystalline ribbons were 50 mm in length, 6 mm in width, and 0.01 mm in thickness, while the copper specimens were 50 mm in length and 0.625 mm in diameter. For Co-Fe-Si-Mn-B-Cr MGs, their nominal sizes were 50 mm×3.5 mm×0.02 mm.

Mentioned configurations (parallelepiped ribbons or cylindrical rods) were selected for the estimation of universal mechanical response in different specimens at the same axial testing conditions. Differential scanning calorimetry (DSC) with heating rate of 5 K/min was used for the detection of glass-transition temperature (T_g) and crystallization temperature (T_x) of Al-Y-Ni-Co, Cu-Pd-P, and Co-Fe-Si-Mn-B-Cr MGs. T_g of Al-Y-Ni-Co, Cu-Pd-P, and Co-Fe-Si-Mn-B-Cr MGs was 533, 528, and 716 K, respectively; T_x of Al-Y-Ni-Co, Cu-Pd-P, and Co-Fe-Si-Mn-B-Cr MGs was 545, 568, and 743 K, respectively. Additionally, the comparison between crystalline and amorphous alloys during the whole deformation experiment was conducted for understanding the role of atomic reorganization under non-isothermal impact.

To estimate the surface tension release state of the specimens after two-fragment fracture, FemtoScan (Advanced Technologies Center) scanning probe microscope, which was

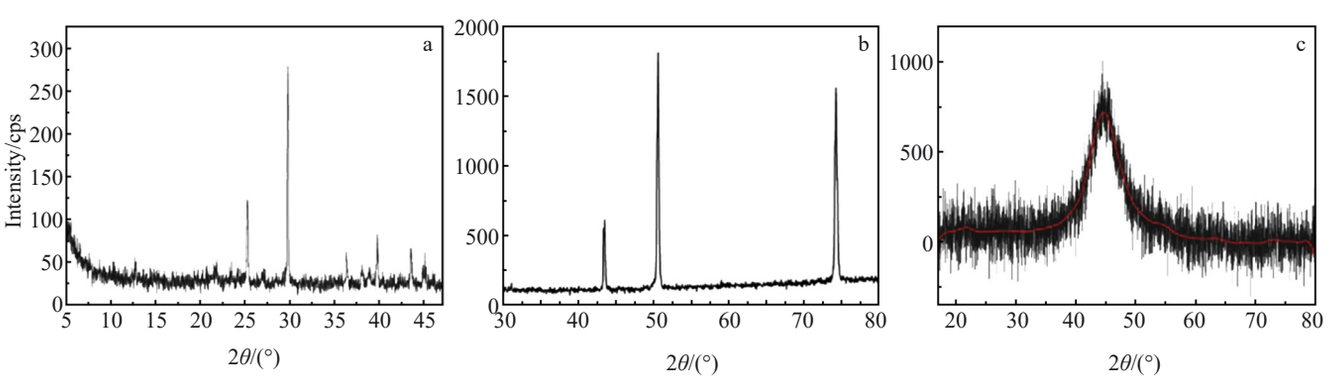

Fig.1 XRD patterns of representative Al-Fe (a), Cu (b), and MG (c)

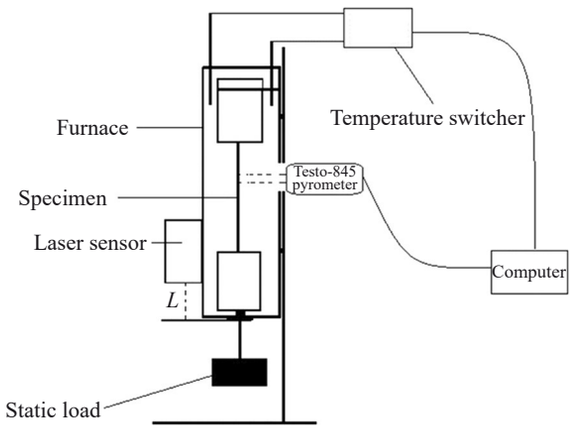

Fig.2 Schematic diagram of creep loading test

operated at the atomic-force microscope (AFM) mode, or Vega3 (Tescan, JCM-7000, Jeol) scanning electron microscope (SEM) was used.

Magnetometry of Co-Fe-Si-Mn-B-Cr ferromagnetic MG was analyzed through the LakeShore 7407 device under the conditions of external magnetic fields of [−9950, 9950] and [−79600, 79600] A·m^2, saturation magnetization of ±80 A·m^2·kg^{-1}, and directions parallel and perpendicular to the specimens before and after deformation tests. Besides, neodymium permanent magnets under the same external magnetic field were used for simultaneous induction of external field in non-isothermal creep tests.

3 Results and Discussion

3.1 Primary analysis of experiments and further generalization

Fig.3 shows experimental TMA and isochronal deformation curves for ribbon and rod specimens of different composition and interatomic structures. DMA qualitatively demonstrates the same deformation dynamics as TMA, as shown in Fig.3.

According to Fig. 3, difference in the deformation rate (during TMA) can be observed, which is caused by both structural features (MG or crystal) and size effect (copper rods are 25 times thicker than Cu-Pd-P ribbons). Despite these differences, interpolation by the empirical fractional function is possible for all experimental data, as expressed by Eq. (1), as follows:

$$x(t) = x_0 + \frac{Ct}{B^2 - Bt} \quad (1)$$

where x_0 (or l_0), C, B, and t are related parameters whose physical meaning and stable dimension are described in Ref.[29,33–35,38]. Eq.(1) shows high correlation coefficient r ($0.9<r<1.0$). For TMA of Al-Y-Ni-Co amorphous alloys, Eq. (1) has to be supplemented by the linear $-Dt$ term ($-D$ indicates the process rate), which is related to reversible shrinkage of a specimen under the static load. All related parameters are listed in Table 1, and the results coincide well with the curves in Fig.3.

According to Table 1, the analysis parameters can accurately describe the deformation situation, and the influence of external experimental conditions on it can reach

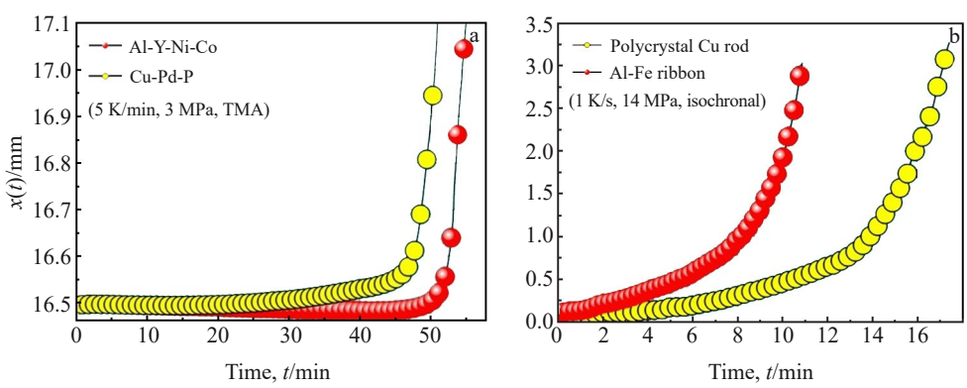

Fig.3 Deformation curves of Al-Y-Ni-Co and Cu-Pd-P amorphous ribbons (a); isochronal test results of polycrystalline Al-Fe ribbon and polycrystal Cu rod (b)

Table 1 Experiment parameters

Composition (alloy type, experiment)	Multiplier, C/ $\times10^{-3}$ m·min	Fracture time, B/min	Shrinkage rate, D/ $\times6\times10^{-2}$ m/s	Linear correlation coefficient, r
Al-Y-Ni-Co (MG, ribbon, TMA)	0.43	55.20	0.000 99	0.970
Co-Fe-Si-Mn-B-Cr (MG, ribbon, isochronal test)	3.90	15.50	0	0.997
Cu-Pd-P (MG, ribbon, TMA)	1.50	52.84	0	0.990
Al-Fe (polycrystal, ribbon, isochronal test)	6.00	12.60	0	0.998
Cu (polycrystal, rod, isochronal test)	8.00	19.50	0	0.996
Al-Y-Ni-Co (MG, ribbon, DMA)	1.30	52.61	0	0.980
Cu-Pd-P (MG, ribbon, DMA)	0.10	47.58	0	0.995

the 10th and 100th decimal places (larger loads and faster heating rates will cause parameter B to decrease as parameter C increases). Moreover, Eq. (1) can solve the ordinary differential Duffing equation, which describes mechanical oscillations of a material under non-linear external conditions[39]. In other words, Eq.(1) is an exact solution of the non-linear homogeneous differential equations $\ddot{x} - P_3(x) = 0$ or $\ddot{x} + c_1x + c_2x^2 + c_3x^3 = 0$, where $P_3(x)$ is a cubic polynomial by x variable with constant coefficients of $c_1 = -6/B^2$, $c_2 = -6/CB$, and $c_3 = -2/C^2$ at x, x^2, and x^3 positive terms, respectively. Besides, $-2C/B$ is the free term. The second temporal derivative of Eq. (1) should be calculated with the further exchange from t to x, using the inverse function relative to Eq.(1), $t = \frac{B^2\Delta x}{C + B\Delta x}$[33]. Then, the derived expression for $\ddot{x}[t(x)]$ is substituted into the abovementioned equations, and the obtained fractions are algebraically simplified by reducing them to a common denominator and performing mutual subtraction of opposite terms. As a result, $\ddot{x} - P_3(x) = 0$ or $\ddot{x} + c_1x + c_2x^2 + c_3x^3 = 0$ turns to the 0=0 state.

These circumstances permit material behaviour analysis via the same model despite different composition and geometry factors. Specific controlling factors are heating rate and external loading, because these factors can accelerate deformation with the appearance of a typical convex $x(t)$ curve. Periodical loading (DMA) leads to the accelerated destruction of Al-Y-Ni-Co amorphous alloy[33], as expressed by Eq.(2).

$$\dot{\varepsilon} l_0 B^2 \approx C \quad (2)$$

where $\dot{\varepsilon}$ is the deformation rate.

Besides, Al-based MG deforms three times slower during TMA than in DMA. Therefore, the value order of the calculated deformation rate is about 10^{-4} s^{-1}. Likewise, the deformation rate of Cu-based MG calculated for DMA exceeds the one for TMA. This phenomenon can be explained by (1.6 times) higher loading in DMA. The presence of $-Dt$ term in TMA of Al-Y-Ni-Co is caused by a reversible decrease in deformation rate, but it does not affect the main reaction force dynamics. This is because further differentiation of Eq. (1) can eliminate this term using Newton's law. Simultaneous induction of the external magnetic field does not noticeably change the deformation dynamics, namely the non-isothermal creep by Eq.(1), below or above Curie temperature T_C. On average, T_C=600 K for investigated Co-Fe-Si-Mn-B-Cr alloys despite the change in integral magnetic response, which is caused by collective spin-orbital relaxation[40] during the test, as indicated in Fig.4.

It is determined that alternative interpolation of the experimental $x(t)$ value by one or three standard exponent functions does not provide the sufficient correlation (≥0.9), as r for exponents is 1.5 times less than the corresponding parameter in Table 1. Thus, Eq. (1) is universally applicable for deformation analysis of different alloys, and the necessary initial experimental conditions are non-zero heating rate and positive (constant, oscillating, or combined) mechanical loading. Deformation mechanisms of amorphous and crystalline materials are qualitatively similar due to the same stage when dislocations or shear bands collectively form identical flow structures. However, specific structural features, such as β-relaxation in MG[41], can also appear during the experiment. Nevertheless, all differences in non-isothermal cases can be quantitatively described by the material parameters C and B through Duffing equation. Isochronal behaviour and TMA differ from isothermal deformation (with an exponential primary stage in the temporal strain curve) because of non-equilibrium thermomechanical reorganization, which is in opposite to Maxwell or Kelvin-Voigt mechanism with the primary dynamics caused by quasi-equilibrium structural changes. This linear heating process accompanied by an increase in static external load will only lead to more severe irreversible deformation of the specimen (without exponential initial stage), and its strength is higher than that in the permanent thermal transfer situation under fixed mechanical load.

3.2 Force-function analysis

It is possible to calculate the main physical and technical parameters in Table 1 for non-isothermal deformation (detail model development and basement are described in Ref.[29,33–34,38]). During TMA, the $A\sin(\omega t)$ harmonic term equals 0 in the reaction force equation of a tested specimen[38], as follows:

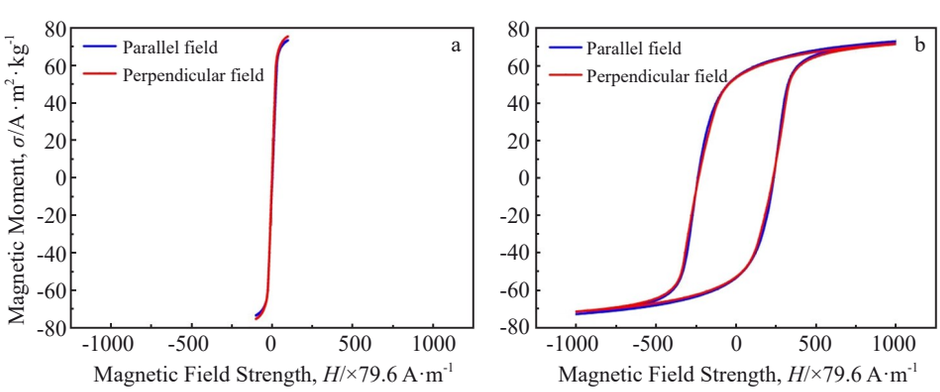

Fig.4 Typical hysteresis loops of Co-Fe-Si-Mn-B-Cr alloy under different conditions: (a) before treatment at room temperature; (b) after non-isothermal creep test at 743 K with further cooling to 300 K with T_C=623 K

$$F_{\text{react.}}[\omega;t(T)]=F_{\text{load}}-A\sin(\omega t)-\frac{2mC}{(B-t)^3} \quad (3)$$

where ω is cyclic frequency; A is amplitude with A=0; m is mass with m=10^{-4} kg; g is gravitational acceleration; other parameters are described in Ref.[38].

Because the fixed loading $F_{\text{load}} = mg$[35], or F_{load} = Const ≠ 0, the $A\sin(\omega t)$ harmonic term equals 0. During the action of linear temporal heating (with a constant heating rate), reaction force in Eq. (3) decreases, and the specimen finally breaks under the fixed load. With the initial elasticity of specimens[38], using the relationship between material stiffness k and its fracture time point B ($k \approx 6m/B^2$ [34]), lag behaviour of δ phase can be analytically estimated under deformation ε, which is related to stress σ during DMA (only the initial experiment stage). Particularly, using $\omega = \varphi/t = \sqrt{k/m}$ (φ is phase) classic wave equations with rough replacement of acting frequency ω by a similar material parameter ($\omega = \varphi/t \approx \delta/t$) provides the $\delta = \omega t \approx t\sqrt{6}/B$ linear expression for time t and lag behaviour of δ phase in the elastic area. This estimation correlates with some part (between t=0 and β-relaxation time) of the δ curve in Ref. [33]. Unlike DMA, as the additional periodical loading is absent, resonance and beating in the specimens[34] do not appear during TMA. These phenomena can be well described by the model, where the harmonic term $A\sin(\omega t)$ is not added to the $\frac{-2mC}{(B-t)^3}$ fractional function. The temporal difference in atomic or molecular reorganization (T_g and T_x) during DSC and DMA tests decreases in TMA test due to static load, but the impact of heating rate on the structural relaxation still exists. The absence of periodical loading also enhances the structural viscosity that is described by less model terms. Derivatives of particular equations by the strain rate have less negative terms if ω = 0, as expressed by Eq.(4–5)[33]:

$$\tau(\dot{\varepsilon}) \approx \frac{F_{\text{load}} - A\omega B + A\omega\sqrt{\frac{C}{l_0}}\dot{\varepsilon}^{-1/2} - 2m\sqrt{\frac{l_0^3}{C}}\dot{\varepsilon}^{3/2}}{hl_0\sqrt{\frac{C}{l_0}}\dot{\varepsilon}^{1/2} - \frac{hC}{B} + hl_0} \quad (4)$$

$$\tau(\dot{\varepsilon}) \approx M - a_1\dot{\varepsilon} - a_2\dot{\varepsilon}^{1/2} - a_3\dot{\varepsilon}^{-1} - \theta(\dot{\varepsilon};a_i) \quad (5)$$

where h is the thickness; $a_1 - a_3$ and M are division factors; $\theta(\dot{\varepsilon};a_i)$ is a remainder (i>3, i is natural number) at division of numerator by the denominator in Eq. (4); other parameters are explained in Ref.[33].

Moreover, in this case, viscosity remains non-Newtonian (due to linearly changing thermal activation). Generalizing thermodynamic and statistical models[29] preserve their relevance and main relationships except for periodical terms. The C and B values, depending on deformation dynamics, also differ in each case.

3.3 Calculation of material parameters under non-isothermal conditions

3.3.1 Linear thermal expansion coefficient

Using the model from Ref. [42], the numerical value of the linear thermal expansion coefficient (CLTE) α_L in TMA can be calculated for alloys via the derivative of Eq. (1) by temperature terms, namely $dx[t(T)]/dT$ and $t = \frac{T - T_0}{V_T}$ (T_0 is the room temperature), which is also linearly related to time. For Al-Y-Ni-Co MG (TMA and T=507 K), α_L=8.6×10^{-6} K^{-1}; for crystalline Al-Fe (deformation at T=507 K), α_L=2.4×10^{-5} K^{-1}. This result agrees well with the magnitude order result in Ref. [43]. Similar numerical parameters, calculated for Cu-based amorphous and crystalline alloys, also agree with the results in Ref. [44], and they vary from 4×10^{-6} K^{-1} (MG) to 7×10^{-6} K^{-1} (polycrystalline) in the temperature interval of 300–500 K. For Co-based MG, α_L=3.4×10^{-6} K^{-1} (T=300–400 K), which agrees well with the result in Ref. [45]. CLTE tends to increase for alloys with the same base components because of different preset heating rates (parameters C and B also depend on heating rate), and alloy configuration leads to α_L(Cu-Pd-P)< α_L(Cu) with mainly thermal elongation of rods without lateral expansion or contraction inherent to ribbons.

3.3.2 Necking and fracture analysis

Laminar and turbulent plastic flow of amorphous alloys were studied through axial experiments with different loads and temperatures[35,42,46]. Presence of viscous homogeneous deformation in ribbon specimens[33] permits the abovementioned model relationships Eq.(1–5) for the further analysis of material necking and fracture with respect to possible nonlinearity. For the estimation of necking form in the ribbon specimen, relationships of elastic plane deformation with the linear heat transfer term[47] are used for analysis:

$$\begin{cases}\varepsilon_{xx} = \dfrac{\sigma_{xx} - \upsilon\sigma_{yy}}{E} + \alpha T \\ \varepsilon_{yy} = \dfrac{\sigma_{yy} - \upsilon\sigma_{xx}}{E} + \alpha T\end{cases} \quad (6)$$

where ε_{xx} and ε_{yy} are diagonal components of strain tensors; σ_{xx} and σ_{yy} are diagonal components of stress tensors; E is Young's modulus of material; α is CLTE; υ is Poisson's ratio; T is temperature. The expression of σ_{yy} via other parameters in Eq. (6) permits the relationship between both deformation projections in the form, as follows:

$$\varepsilon_y(\varepsilon_x) = \frac{\sigma_x - (\varepsilon_x - \alpha T)E - \upsilon^2\sigma_x}{\upsilon E} + \alpha T \quad (7)$$

where ε_x and ε_y are components of strain tensors; σ_x and σ_y are components of stress tensors. The further substitution of all material constants in Eq.(7) usually gives a linear deformation contour with about 45°, which is well-known for traditional stretch tests. However, those values change during experiments, such as CLTE and temperature with $\varepsilon_x \sim x(t) \sim l(t)$. Consequently, corresponding temporal and temperature functions are adopted for Eq.(7) with substitution of $t = \frac{B^2\Delta l}{C + B\Delta l} = \frac{T - T_0}{V_T}$[33] and addition of $\upsilon \to 0$ if $t \to B$ instead the fixed parameters (α, T, E, υ). It specifies the plastic flow contour (necking) at the final experiment stage, i.e., not only the elastic stage. As the precise dynamics of Poisson's ratio is obscure in this experiment (except its initial value), the Poisson's ratio is used for the second variable (with the temperature). Thus, the main view of possible necking profiles

$\varepsilon_y = f(x; \upsilon)$ is plotted, as shown in Fig. 5. The elastic and viscous contours are mentioned by blue and green curves, respectively.

According to Fig. 5, the non-linear necking profile (a projection on the $f(x; y)$-elongation plane) can be observed, which can be further testified by SEM and optical microscope (Fig.6).

Fig. 6 shows fracture morphologies of different specimens after TMA and static load. It can be inferred that necking contour of rods (cylinders) should be considered in Eq. (7), because Eq. (6) should be reorganized in the cylindrical coordinates. As shown in Fig. 6b, the corrugation of ribbon appears due to step-by-step crack from edge to the center. Eq. (6) cannot be used for a description of this effect because its derivation is conducted in continuum mechanics. For the deformation based on Eq. (6), power expression between the σ_{yy} lateral stress and ε_{xx} longitudinal strain (depending on transverse crack contour length) can be found. Moreover, the fatigue Paris-Erdogan formula[48] can be derived under the mentioned conditions. For this purpose, the first term in Eq. (6) was used with the further substitution of deformation rate instead $\varepsilon_{xx} = \varepsilon_x$ (via recurrent equation $\varepsilon_x = \sqrt{\frac{C\dot{\varepsilon}_x}{x_0}} - \frac{C}{Bx_0}$ between $\dot{\varepsilon}_x$ and ε_x[35]). Finally, the required $\dot{\varepsilon}_x(\sigma_y)$ equation will be obtained, as follows:

$$\dot{\varepsilon}_x = J - b\sigma_y^2 \sim \sigma_y^\beta \tag{8}$$

where J and b are constants; β is a power parameter. According to Eq. (8), a fracture crack growth occurs in TMA and isochronal experiments, similarly to fatigue tests from the model standpoint. This conclusion is experimentally approved by SEM, as shown in Fig.7.

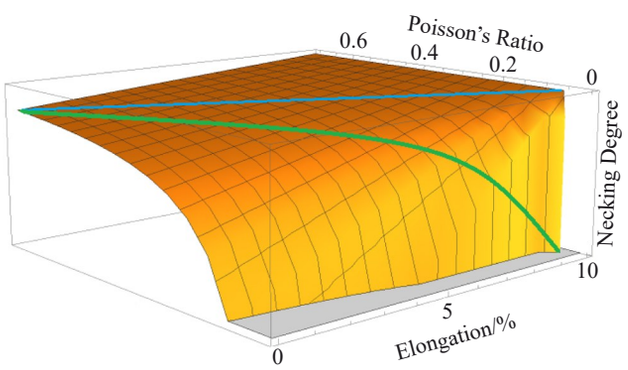

Fig.5 Surface of potential deformation profiles of specimen

In the crack propagation process, typical fatigue characters, such as cavity (white arrow), ligament (green arrow), sharpening transgranular fracture (red arrow), and angular stress striation (blue arrow) can be observed[49], as shown in the inset in Fig.7.

3.3.3 Corrugation and analysis

Eq. (6) cannot describe the corrugation of specimen, because it contains a discontinuity (the growing fracture crack). Thus, the corrugation-applied models, such as Euler-Bernoulli beam theory[50], cannot be used for the current task, or they have to be combined as a step-by-step equation system for every moment of the fracture stage. Moreover, there are real overlapping (addible or subtractable) corrugated material waves, resulting in difficult description by the neutral axis approximation shifts or breaks relative to ε_y at the last deformation stage (until the final fracture). Except for the corrugation in MG (Fig. 8a), texturing (Fig. 8b), namely the formation of micro-crack or pore netting with boundary (Fig. 8c) and complex release (±1.3 μm, Fig. 8d), occurs in Al-Fe polycrystalline ribbons during TMA and static load deformation. Fig. 8b shows the transition boundary between smooth and corrugated areas, which is marked by the red circle. The transition boundary is also indicated by the red arrows in Fig.8c.

For the deformation of Al-Fe specimens, texturing can appear along coarse grain boundaries, or sub-fragmentation of the polycrystalline structure is also possible. As an alternative model approach, fractal analysis[51] and reference fractal dimension index n can be used for a structural description of ribbon at the fracture stage (with corrugation). From this standpoint, the development of every fold is considered as the percolation (progressive defect distribution), embracing some particles in the specimen structure. Thus, Eq. (9) can be obtained for the calculation of a specific percolation element size[51]:

$$\xi \sim [P(T) - P_0]^{-n} \tag{9}$$

where ξ is relative element size; $P(T) - P_0$ is probability change. The corrugation scale can be estimated. According to Ref.[29], the probability distribution function is as follows:

$$\alpha_0 + (\alpha_1 + \alpha_2)\exp(\tau) + \alpha_3 \exp(4\tau) \sim f(T) \tag{10}$$

where α_k (k=0 – 3) is exponential coefficient; τ =

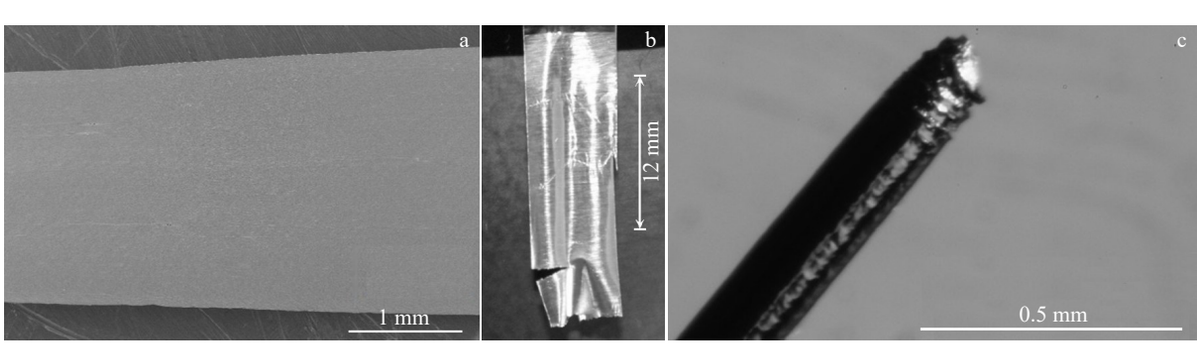

Fig.6 Fracture morphologies of different specimens after TMA and static load: (a) Cu-Pd-P ribbon MG with linear fracture profile; (b) Al-Fe ribbon with non-linear fracture; (c) polycrystalline Cu rod with non-linear cigar-shaped edging contour

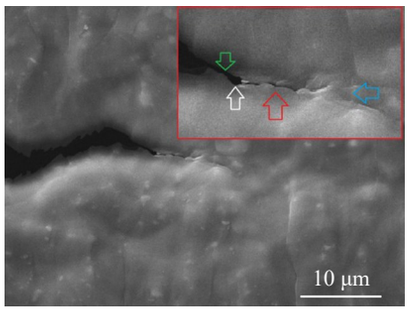

Fig.7 SEM image of lateral crack in Al-Fe specimen during stretch test with inset of crack tip

$\int \frac{\mathrm{d}T}{V_T\left(B-\frac{T-T_0}{V_T}\right)}$; other parameters are described in Ref.[29].

The probability distribution function under different temperatures and mechanical loadings should be adopted in Eq. (9) instead of $P(T)-P_0$, because it considers the necessary experiment data (Table 1). Considering the fractal index of glass and amorphous polymers n≈0.8[52], within the temperature range of 300–600 K, the required relative element size can be determined to be 10^{-2} m. The calculated ξ values are in agreement with the results of magnitude order of length of ribbon and longitudinal corrugation fold, which proves the self-similarity of the formation of the wrinkles and their non-linear expansion characteristics.

As bulk specimens do not undergo corrugation (only brittle fracture occurs[53]) under the similar conditions[54], the optimal (minimal) thickness without this effect is necessary. Since the Reynolds number (Re) is the typical ratio for estimation of laminar and turbulent (non-linear) flow or deformation regime[55], it is adopted in this research. Additionally, in Ref. [42], the temporal relation between this value and non-linear deformation of ribbon amorphous specimens was determined, as follows:

$$Re=\frac{\dot{x}\rho s}{\eta}=\frac{m\dot{x}s}{V\eta}=\frac{m\dot{x}(t)}{ax(t)\eta(t)} \tag{11}$$

where a and s are thickness and width, respectively; ρ is density of specimen; $\dot{x}$ or $\dot{x}(t)$ is deformation rate; η is dynamic viscosity; V is volume of a system; other parameters are described in Ref. [42]. By substituting Eq. (1) and its derivative into Eq. (7), the Reynolds number can be determined as a function of thickness and time, Re=f(a; t). Considering that Re/Re_0 is about 4000–6000 (in this case, the specimen becomes to plastic flow state[42]) at time t~B, the magnitude order of parameter a (Re/Re_0 acceleration is minimal) can be determined, as shown in Fig.9. The boundary temporal point of the stable function area (beyond 0.3 mm, the surface does not practically change) is indicated by the red line. The optimum thicknesses for Cu-Pd-P and Al-Fe ribbons

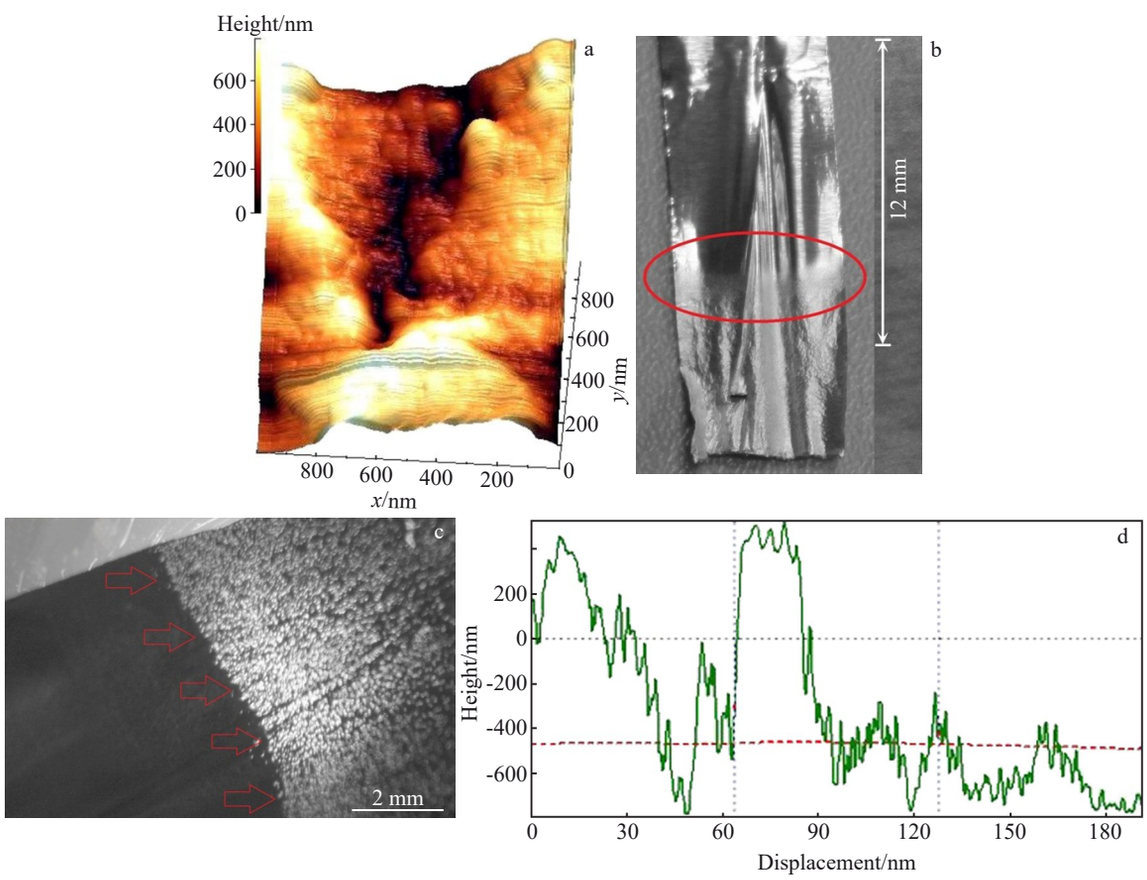

Fig.8 Corrugation and texturing of specimens in TMA and isochronal tests: (a) AFM surface of Cu-Pd-P MG; (b) Al-Fe ribbon after fracture with crinkled form; (c) appearance of Al-Fe ribbon; (d) AFM profile near the fracture line of Al-Fe ribbon

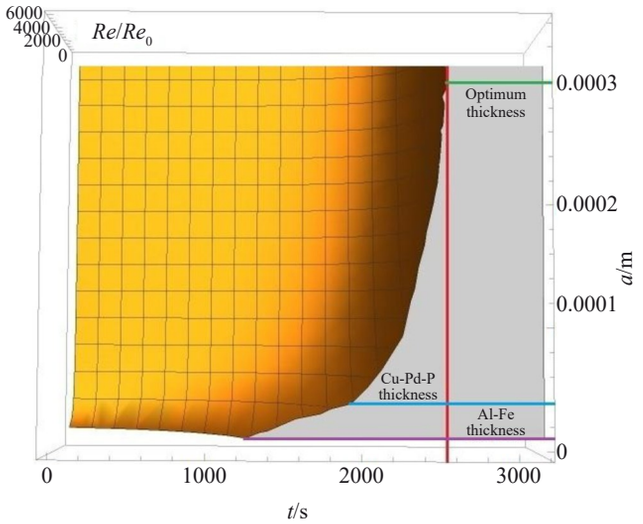

Fig.9 Schematic diagram of $Re(a;t)$ surface

are indicated by green, blue, and violet lines in Fig.9 (Al-Y-Ni-Co and Co-Fe-Si-Mn-B-Cr specimens have the same thickness order as that of Al-Fe).

Thus, According to Eq. (11), the optimal thickness $a \geqslant 0.3$ mm without corrugation can be found, i. e., the specimens must be 15 – 30 times thicker than the considered ones if a more stable deformation is needed. It is known that Cu-Pd-P ribbon specimens (thickness of 0.025 mm) undergo corrugation[42], which agrees with the calculated unstable flow area in Fig. 9. Additionally, the diameter of polycrystalline Cu rods is about 0.625 mm, and corrugation cannot be observed (fracture without visible longitudinal folds). In Fig. 9, the bottom (zero) limit of thickness can be observed, where Re/Re_0 cannot be calculated due to its function gap that has the physical meaning. This result testifies the adequacy (lower limit) of the proposed model.

4 Conclusions

1) Similarity among TMA, DMA, and isochronal test exists, and it can be described in form of the same meso-physical model using the non-linear Duffing equation for axial oscillations of a material point, despite the specimen geometry or interatomic structure.

2) Quantitative description can be obtained with model parameters C and B, providing the maximum correlation with the experiment. Calculation of important thermodynamic characteristics is possible with necking and fracture analysis. All derived values and their numerical data are in good agreement with the experiment results. Thus, the proposed model and approaches can be used for all materials with the same deformation behaviour under the conditions mentioned in this research.

Acknowledgement

Dr. Arseniy Berezner thanks dear Monsieur Schabot Lucien Georges from Grand-Duché de Luxembourg for comprehensive and perennial help, making it possible to realize this work. The results were partially obtained at the Center for Collective Use of Scientific Equipment at Derzhavin Tambov State University. Magnetometry test was performed at Magnetic Materials Research Laboratory (Lomonosov Moscow State University).

References

1 Yang X X, Xiao G S, Zhang S B *et al*. *Engineering Fracture Mechanics*[J], 2024, 305: 110195
2 Ma Y H, Liu C L, Miao K S *et al*. *Journal of Alloys and Compounds*[J], 2023, 947: 169559
3 Wen C Y, Tang J, Chen W T *et al*. *Journal of Alloys and Compounds*[J], 2023, 965: 171006
4 Liu X K, Wang T C, Wang Q P *et al*. *Intermetallics*[J], 2022, 140: 107378
5 Liang S Y, Zhu F, Wang Y J *et al*. *International Journal of Engineering Science*[J], 2024, 205: 104146
6 Louzguine-Luzgin D V. *Materials*[J], 2024, 17(14): 3573
7 Meyers M, Chawla K. *Mechanical Behavior of Materials*[M]. Cambridge: Cambridge University Press, 2008
8 Suryanarayana C, Inoue A. *Bulk Metallic Glasses*[M]. Boca Raton: CRC Press, 2020
9 Rees D. *Basic Engineering Plasticity*[M]. Amsterdam: Butterworth-Heinemann, 2006
10 Mizzi L, Salvati E, Spaggiari A *et al*. *International Journal of Mechanical Sciences*[J], 2020, 167: 105242
11 Louzguine-Luzgin D, Zadorozhnyy M, Ketov S *et al*. *Materials Science and Engineering A*[J], 2019, 742: 526
12 Xu Y Q, Zhan L H, Huang M H *et al*. *Journal of Materials Processing Technology*[J], 2018, 255: 26
13 Menard K. *Dynamic Mechanical Analysis: A Practical Introduction*[M]. Boca Raton: CRC Press, 1999
14 Xue R J, Zhao L Z, Yi J J. *Materials Letters*[J], 2022, 306: 130931
15 Zadorozhnyy V, Zadorozhnyy M, Churyumov A *et al*. *Physica Status Solidi A*[J], 2016, 213: 450
16 Vlasak G, Svec P, Duhaj P. *Materials Science and Engineering A*[J], 2001, 304–306(1): 472
17 Gyurov S, Czeppe T, Drenchev L *et al*. *Materials Science and Engineering A*[J], 2017, 684: 222
18 Lei C, Li H, Fu J *et al*. *Materials Characterization*[J], 2018, 144: 431
19 Wu X T, Zhan L H, Yang Y L *et al*. *Metals*[J], 2023, 13(1): 409
20 Kachanov L M. *Introduction to Continuum Damage Mechanics*[M]. Berlin: Springer, 1986
21 Kachanov L. *Creep in Structures*[M]. Berlin: Springer-Verlag, 1981
22 Rabotnov Y. *Creep Problems in Structural Members*[M]. Hoboken: Wiley, 1969
23 Birosca S, Liu G, Ding R G *et al*. *International Journal of Plasticity*[J], 2019, 118: 252

24 Anderson P W. *Science*[J], 1995, 267(5204): 1615
25 Spaepen F. *Acta Metallurgica*[J], 1977, 25(4): 407
26 Yu H B, Wang W H, Bai Y Y *et al*. *Physical Review B*[J], 2010, 81(22): 220201
27 Wang J. *International Journal of Hydrogen Energy*[J], 2008, 33(21): 6339
28 Perez J. *Journal of Food Engineering*[J], 1994, 22(1): 89
29 Berezner A, Fedorov V. *Materials*[J], 2022, 15(23): 8659
30 N'souglo K, Rodríguez-Martínez J, Cazacu O. *International Journal of Plasticity*[J], 2020, 128: 02656
31 Wang M, Fourmeau M, Zhao L *et al*. *Proceedings of the National Academy of Sciences*[J], 2020, 117: 16872
32 Louzguine-Luzgin D, Inoue A. *Journal of Alloys and Compounds*[J], 2005, 399(1): 78
33 Berezner A, Fedorov V, Zadorozhnyy M. *Journal of Alloys and Compounds*[J], 2022, 923: 166313
34 Berezner A, Fedorov V, Zadorozhnyy M *et al. Theoretical and Applied Fracture Mechanics*[J], 2022, 118: 103262
35 Fedorov V, Berezner A, Beskrovnyi A *et al. Technical Physics Letters*[J], 2018, 44: 678
36 Zhang T, Zhao N N, Li J C *et al. RSC Advances*[J], 2017, 7: 23583
37 Narushima T, Tsukamoto H, Yonezawa T. *AIP Advances*[J], 2012, 2: 042113
38 Berezner A, Fedorov V, Zadorozhnyy M *et al. Metals*[J], 2021, 11(6): 908
39 Jordan D, Smith P. *Nonlinear Ordinary Differential Equations*[M]. Oxford: Oxford University Press, 2007
40 Berezner A, Fedorov V, Perov N *et al. Journal of Physics: Condensed Matter*[J], 2019, 32: 114001
41 Wang W H. *Progress in Materials Science*[J], 2019, 106: 100561
42 Berezner A, Fedorov V, Grigoriev G. *Lecture Notes in Mechanical Engineering*[M]. Berlin: Springer, 2022
43 Li G H, Wang W M, Bian X F *et al. Materials Chemistry and Physics*[J], 2009, 116(1): 72
44 Wang Y Y, Bian X F, Jia R. *Transactions of Nonferrous Metals Society of China*[J], 2011, 21(9): 2031
45 Teslia S, Solodkyi I, Yurkova O *et al. Journal of Alloys and Compounds*[J], 2022, 921: 166042
46 Wu G, Liu S, Wang Q *et al. Nature Communications*[J], 2023, 14: 3670
47 Dugdale D. *Elements of Elasticity*[M]. Oxford: Pergamon Press, 1968
48 Paris P, Erdogan F. *Journal of Basic Engineering*[J], 1963, 85(4): 528
49 Milella P. *Fatigue and Corrosion in Metals*[M]. Berlin: Springer, 2013
50 Heshmati M, Daneshmand F, Amini Y. *Ocean Engineering*[J], 2023, 271: 113507
51 Feder J. *Fractals*[M]. Berlin: Springer, 1988
52 Ozhovan M. *Journal of Experimental and Theoretical Physics*[J], 2006, 103(5): 819
53 Qu R T, Volkert C, Zhang Z F *et al. Journal of Materials Science & Technology*[J], 2023, 149: 247
54 Sun B A, Wang W H. *Progress in Materials Science*[J], 2015, 74: 211
55 Landau L, Lifshitz E. *Fluid Mechanics*[M]. Amsterdam: Butterworth-Heinemann, 1987

不同空间构型或结构状态的铝、钴和铜基合金的非等温流动：模型建立与实验

Berezner Arseniy Dmitrievich[1]，Fedorov Victor Alexandrovich[1]，Perov Nikolai Sergeevich[2]，乔吉超[3]，Gromov Victor Evgenievich[4]，Zadorozhnyy Mikhail Yurievich[5]，Gregory Victorovich Grigoriev[1]

(1. 德扎文钦坦博夫国立大学 理论与实验物理系，俄罗斯 坦博夫 392000)

(2. 洛蒙佐夫莫斯科国立大学 磁学系，俄罗斯 莫斯科 119991)

(3. 西北工业大学 力学与交通运载工程学院，陕西 西安 710072)

(4. 西伯利亚国立工业大学 自然科学系，俄罗斯 诺沃库涅茨克 654007)

(5. 国家科技大学 功能高分子材料实验室，俄罗斯 莫斯科 119049)

摘　要：通过构建新变形模型为不同合金的非等温行为提供了通用描述方法。结果表明，预测模型与实验结果之间存在很强的相关性，这表明对主要应用参数（如线性热膨胀系数）的预测是准确的。同时，还可以计算出带状和棒状试样的颈缩轮廓和波纹的临界厚度。对多晶和无定形带状试样的波纹褶皱进行了形状分析（主要尺寸）。研究了塑性变形阶段的结构特征。

关键词：金属玻璃；热分析；热膨胀；扫描电子显微镜

作者简介：Berezner Arseniy Dmitrievich，博士，德扎文钦坦博夫国立大学理论与实验物理系，俄罗斯 坦博夫 392000，E-mail：a.berezner1009@gmail.com